

1 **Pore network model predictions of Darcy-scale**
2 **multiphase flow heterogeneity validated by experiments**

3 **Christopher Zahasky¹, Samuel J. Jackson¹, Qingyang Lin¹, Samuel Krevor¹**

4 ¹Department of Earth Science and Engineering, Imperial College London, London, England

5 **Key Points:**

- 6 • Pore network models extracted from X-ray micro-computed tomography scans can
7 predict capillary heterogeneity in subdomains of core samples.
- 8 • Darcy-scale simulation results, parameterized with pore network model output,
9 agree well with independent experimental measurements.
- 10 • A digital rocks approach is presented for multiphase characterization that requires
11 no experimental calibration.

Corresponding author: Christopher Zahasky, chris.zahasky@gmail.com

Abstract

Small-scale heterogeneities in multiphase flow properties fundamentally control the flow of fluids from very small to very large scales in geologic systems. Inability to characterize these heterogeneities often limits numerical model descriptions and predictions of multiphase flow across scales. In this study, we evaluate the ability of pore network models (PNM) to characterize multiphase flow heterogeneity at the millimeter scale using X-ray micro-computed tomography images of centimeter-scale rock cores. Specifically, pore network model capillary pressure and relative permeability output is used to populate a Darcy-scale numerical model of the rock cores. These pore-network-derived Darcy-scale simulations lead to accurate predictions of core-average relative permeability, and water saturation, as validated by independent experimental datasets from the same cores and robust uncertainty analysis. Results highlight that heterogeneity in capillary pressure characteristics are more important for predicting local and upscaled flow behavior than heterogeneity in permeability or relative permeability. The leading uncertainty in core-average relative permeability is driven not by the image processing or PNM extraction, but rather by ambiguity in capillary pressure boundary condition definition in the Darcy scale simulator. This characterization workflow enables predictions of local capillary heterogeneity and core-averaged multiphase flow properties while circumventing the need for the most complex experimental observations conventionally required to obtain these properties.

1 Keywords

digital rock physics, pore network model, capillary heterogeneity, X-ray computed tomography, multiphase flow

2 Plain Language Summary

To understand how fluids flow in subsurface rocks it is often necessary to perform laborious and expensive experiments aimed at replicating the subsurface pressure and temperature conditions. In this study, we propose and test a new modeling-based approach using high-resolution images capable of describing the structure and pore space of the rock at a resolution ten times smaller than the width of a typical human hair. We show that with these high-resolution images, along with a few routine rock property measurements, it is possible to predict the distribution of fluids in the rocks at range of sub-

43 surface fluid flow conditions. This digital, or experiment-free, approach has the poten-
44 tial to redefine how we parameterize larger-scale models of problems such as contami-
45 nant flow in aquifers or carbon dioxide migration and trapping in carbon capture and
46 storage reservoirs.

47 **3 Introduction**

48 Multiscale heterogeneity, intrinsic to permeable geologic media, dictates single and
49 multiphase fluid flow across a range of applications in hydrogeology and subsurface en-
50 ergy resource development (P. S. Ringrose et al., 1993; Fehley et al., 2000; Kang et al.,
51 2017; C. A. Reynolds et al., 2018; Cowton et al., 2018). The reservoir-scale impacts of
52 heterogeneous features below the resolution of typical reservoir model grid blocks lead
53 to major challenges in predicting and history matching CO₂ storage and non-aqueous
54 phase liquid migration in the subsurface (P. Ringrose et al., 2009; V. Singh et al., 2010;
55 Eiken et al., 2011). Inability to characterize small-scale heterogeneity limits the predic-
56 tive ability of existing digital rock approaches (Guice et al., 2014).

57 Advances in high-resolution X-ray micro-computed tomography (micro-CT) have
58 enabled new methods for quantifying single and multiphase fluid flow at the pore scale.
59 Micro-CT has been a valuable tool for experimental characterization of pore space ge-
60 ometry, (Lin et al., 2016) mineralogy (Lai et al., 2015; Menke et al., 2015; Beckingham
61 et al., 2017; Al-Khulaifi et al., 2019), wettability (Iglauer et al., 2012; Bartels et al., 2019;
62 Lin et al., 2019), residual trapping (Herring et al., 2013; Chaudhary et al., 2013; Al-Menhali
63 & Krevor, 2016; Øren et al., 2019), and curvature-based capillary pressure (Armstrong
64 et al., 2012; Herring et al., 2017; Garing et al., 2017; Lin et al., 2018; T. Li et al., 2018).
65 Increased availability of affordable high-power computational and data management re-
66 sources have enabled micro-CT imaging to increasingly be used to image centimeter-scale
67 samples with voxel resolutions less than 10 micrometers (Lin et al., 2018; S. J. Jackson
68 et al., 2019; Øren et al., 2019).

69 Models to describe fluid flow at the pore scale can be roughly categorized as di-
70 rect simulation methods and pore network methods. In direct simulation methods, the
71 Navier-Stokes equations are solved on a grid defined by the pore structure of the sam-
72 ple using finite difference, finite element, or Lattice-Boltzmann methods. Alternatively,
73 pore network models (PNM) approximate the pore-space as a construction of optimal

74 shapes—such as balls and tubes—and use continuum solutions of the Navier-Stokes equa-
75 tion to describe fluid flow. By using Navier-Stokes continuum approximations of fluid
76 flow in the pore space, pore network models are able to achieve orders of magnitude faster
77 computational times than direct simulation methods (Raeini et al., 2015; Bultreys et al.,
78 2016; Zhao et al., 2019), and therefore have the potential to run centimeter-scale sam-
79 ple domains. Pore network models have been used to study an array of processes in porous
80 media such as solute transport (Bijeljic et al., 2004; Mehmani & Tchelepi, 2017), mul-
81 tiphase displacement behavior (Chen & Wilkinson, 1985; Lenormand et al., 1988; Idowu
82 & Blunt, 2010; J. Li et al., 2017), diffusion-driven transport (De Chalendar et al., 2018),
83 capillary pressure characteristic behavior (Bakke & Øren, 1997; Vogel et al., 2005; Silin
84 & Patzek, 2006; Hussain et al., 2014), and relative permeability (M. Blunt & King, 1991;
85 Jerauld & Salter, 1990; M. J. Blunt, 1997; Rajaram et al., 1997; Nguyen et al., 2006; Sheng
86 & Thompson, 2016; Berg et al., 2016). However, computation and experimental com-
87 plexity has limited PNM testing and validation to synthetic models (Hilpert & Miller,
88 2001), millimeter-scale experimental samples, or partial sample analysis (Guice et al.,
89 2014). As a result, the ability for pore network models to describe and predict Darcy-
90 scale multiphase flow heterogeneity has not yet been tested or validated against exper-
91 imental measurements in centimeter-scale cores.

92 One of the biggest challenges with modeling natural systems at any scale is the un-
93 certainty that arises from measurements, characterization, and mathematical descrip-
94 tions of complex systems (Pianosi et al., 2016). When using pore network modeling to
95 describe fluid flow in porous media, uncertainty arises in experimental observations (Bultreys
96 et al., 2018), image resolution and processing (Arns et al., 2001; Wildenschild & Shep-
97 pard, 2013; Leu et al., 2014; Berg et al., 2018; A. Singh et al., 2018), network extraction
98 and descriptions (Joekar-Niasar et al., 2010; Dong & Blunt, 2009; Lindquist et al., 2004;
99 Jiang et al., 2007; Mehmani & Tchelepi, 2017), and flow modeling or characteristic curve
100 development (Silin & Patzek, 2006). Current methods to characterize multiscale mul-
101 tiphase heterogeneity in geologic systems are often nonunique, expensive, laborious, and
102 require restricting assumptions (C. Reynolds & Krevor, 2015; Zahasky & Benson, 2018).
103 The resulting experimental and modeling uncertainty has often restricted workflows to
104 tuning pore network or continuum scale models to experimental results, thus limiting
105 their predictive ability.

106 In this study, we describe an approach for building heterogeneous multiphase Darcy-
 107 scale models of centimeter-scale cores utilizing pore network model predictions of char-
 108 acteristic curves in REV subdomains. The approach of using pore network models to char-
 109 acterize heterogeneity in REV subdomains, rather than entire samples, is intrinsically
 110 parallelizable and scalable to larger sample sizes. Uncertainty analysis is used to demon-
 111 strate that the capillary heterogeneity is greater than the uncertainty in pore network
 112 model capillary entry pressure that arises from variations in image processing. This ap-
 113 proach utilizes only published contact angle and interfacial tension data, mercury injec-
 114 tion capillary pressure (MICP) curves, and dry micro-CT scans for pore network model
 115 (PNM) extraction and flow. Comparing Darcy-scale fluid saturation results of this hy-
 116 brid modeling approach with experimentally measured fluid saturations during multi-
 117 phase drainage experiments in the same cores provides an independent means to test the
 118 predictive ability of the pore network models to describe Darcy-scale flow heterogene-
 119 ity. This approach, combined with robust sensitivity analysis, provides a foundation for
 120 future multiscale, multiphase characterization of geologic porous media without the need
 121 for the most laborious and expensive components of traditional multiphase flow char-
 122 acterization.

123 4 Methods

124 4.1 Overview

125 The key data required to build and test the workflow in this study—summarized
 126 in Figure 1—are high resolution X-ray micro-computed tomography images acquired by
 127 S. J. Jackson et al. (2019). Dry scans describe the pore-scale geometry of two centimeter-
 128 scale Bentheimer cores (*Dry Scan* plot in Figure 1). Bentheimer was selected for this study
 129 because of its stability and large pore size. One sample had subtle heterogeneity, while
 130 the other sample had clear sedimentary laminations oriented obliquely to the axis of the
 131 core.

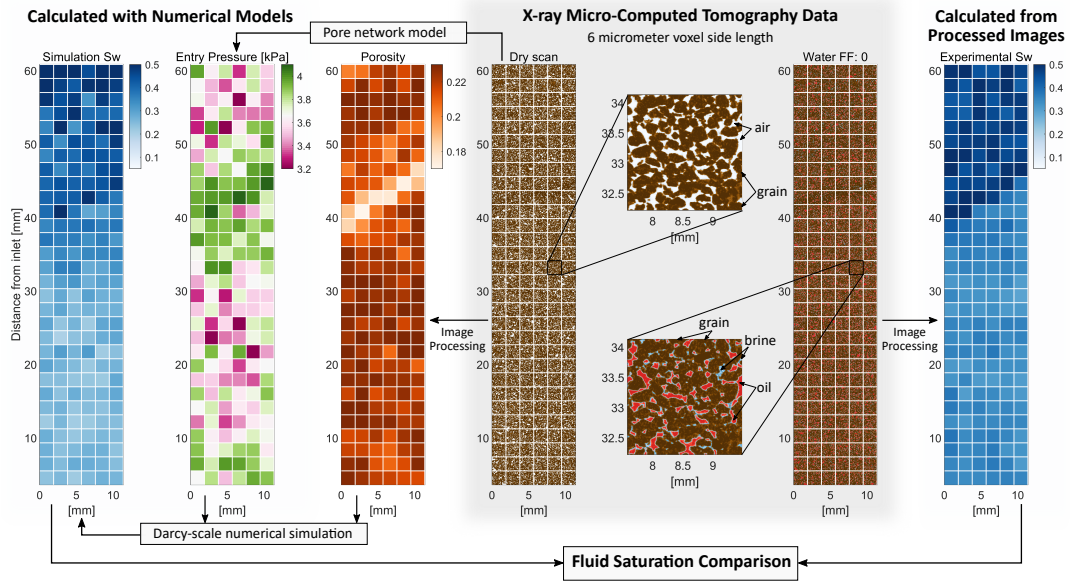
132 The first step in the workflow was to discretize the dry scans into representative
 133 elementary volume (REV) subdomains and segmented to calculate Darcy-scale poros-
 134 ity (*Porosity* plot in Figure 1). This discretization was done to enable unlimited paral-
 135 lelization of the workflow and reduce the computational burden of working with large
 136 datasets. The dry micro-CT image sizes of the full samples used in this study were over

137 60 GB each. Segmented subdomain blocks from the dry scan were run through a pore
 138 network model to estimate capillary entry pressure (*Entry Pressure* plot in Figure 1) and
 139 relative permeability. The porosity and PNM-derived multiphase characteristic curves
 140 in each subdomain were used to parameterize each grid cell of a Darcy-scale numerical
 141 model.

142 To assess the validity of pore network model multiphase characteristic curve pre-
 143 dictions, fluid saturation simulation output from the Darcy-scale model (*Simulation S_w*
 144 in Figure 1) is compared with experimentally measured fluid saturations at equivalent
 145 flow rate conditions. Micro-CT scans at a range of fraction flow conditions (*Water $FF:0$*
 146 example shown in Figure 1) are used to calculate local Darcy-scale fluid saturations in
 147 discrete subdomains of the cores (*Experimental S_w* plot in Figure 1). This independent
 148 comparison between experimentally measured water saturation, and numerically sim-
 149 ulated water saturation in equivalent subdomains provides a means to evaluate the pre-
 150 dictive ability of uncalibrated pore network models to describe Darcy-scale multiphase
 151 flow behavior.

160 4.2 Core Samples and Experiment Description

161 Two Bentheimer cores were utilized in this study. The first, a relatively homoge-
 162 neous core (hereafter referred to as Core 1), was 1.24 cm in diameter and 7.32 cm long.
 163 A second core was selected because it had clear sedimentary lamination, providing the
 164 opportunity to study layered heterogeneities (hereafter referred to as Core 2). Core 2
 165 was 1.24 cm in diameter and 6.47 cm long. The micro-CT image acquisition and mul-
 166 tiphase flow experiments are described in detail in S. J. Jackson et al. (2019). Briefly,
 167 the cores were first loaded into a custom fabricated PEEK coreholder with stainless steel
 168 end caps. A Zeiss Versa 510 CT scanner was used to acquire dry scans of nearly the en-
 169 tire volume of each core with $6\ \mu\text{m}$ cubic voxel side length. Following the completion of
 170 dry scans, the cores were saturated with doped brine such that the drainage experiments
 171 started at fully water saturated conditions. The permeability was measured from mul-
 172 tiple single-phase flow rates and found to be 1635 mD and 763 mD in Core 1 and 2, re-
 173 spectively. Steady-state co-injection of brine and decane was performed at water frac-
 174 tional flows of 0.95 and 0 in Core 1, and 0.95, 0.5, and 0 in Core 2. Scan time and data
 175 management considerations prevented experimental measurements at additional fractional
 176 flow increments. The total flow rate in all experiments was 0.1 mL/min. Decane was used



152 **Figure 1.** A methodological overview and illustration of the data set for Core 2 utilized in
 153 this study. The gray box highlights center-slice micro-CT scans along the axis of the core dur-
 154 ing dry and drainage multiphase flow at a water fractional flow equal to zero. To the left of the
 155 micro-CT data is the resulting Darcy-scale porosity (from image processing), capillary entry
 156 pressure (from PNM), and simulated water saturation. To the right of the micro-CT data is the
 157 Darcy-scale water saturation calculated from image processing of the multiphase micro-CT data
 158 at the same water fraction flow. In the experiments and models fluid is injected from bottom to
 159 top.

177 as the nonwetting phase fluid to minimize the density contrast with water. In addition,
 178 the higher viscosity of decane relative to gaseous nonwetting phases maximizes fluid sta-
 179 bility during the multi-hour X-ray micro-CT scans (C. A. Reynolds et al., 2017). Once
 180 the differential pressure stabilized at each fractional flow, a scan was taken of nearly the
 181 entire core with a $6\ \mu\text{m}$ cubic voxel size. Imaging artifacts arising from the stainless steel
 182 coreholder end caps limited the scan length of the Core 1 to 6.48 cm and the scan length
 183 of Core 2 to 5.69 cm. To acquire micro-CT datasets 6.48 and 5.69 cm in total length,
 184 12 and 10 separate scans were taken in the Core 1 and 2, respectively.

185 **4.3 Full-core Image Reconstruction**

186 Image reconstruction was first performed with the Zeiss reconstruction software to
 187 correct for beam-hardening and center-shift artifacts. Following reconstruction, the multi-
 188 scan images were re-normalized, registered, merged, and cropped using the workflow de-
 189 scribed in detail in S. J. Jackson et al. (2019). This workflow produced a raw 16-bit grayscale
 190 micro-CT image of each core during the dry and multiphase scans. The final image sizes
 191 were $950 \times 950 \times 10,800$ voxels (76.4 GB) and $954 \times 954 \times 9,540$ voxels (64.1 GB) in
 192 Core 1 and Core 2, respectively.

193 **4.4 Image Processing and Pore Network Modeling**

194 ***4.4.1 Pore Network Modeling and Network Extraction***

195 An array of pore network extraction and simulation options are available for a grow-
 196 ing range of pore-scale applications. In this study the maximal ball method described
 197 by Dong and Blunt (2009) is utilized with the free, open-source network extraction al-
 198 gorithm (PNextract) developed by Raeini et al. (2017). As implemented, no assumptions
 199 are made about the topology of the network. Features such as coordination number and
 200 throat geometry are calculated automatically and have been previously validated (Dong
 201 & Blunt, 2009).

202 The pore network model simulations were run using the approach of (Valvatne &
 203 Blunt, 2004) with the updated algorithm (PNflow) described in Raeini et al. (2018) and
 204 further validated by Bultreys et al. (2018); Raeini et al. (2019). This model relies on an
 205 assumption of quasi-static capillary dominated flow. Capillary pressure during drainage
 206 is based on fluid interface force balances using the Mayer-Stowe-Princen method (Mason

207 & Morrow, 1991). See references for additional details of model extraction and formu-
 208 lation.

209 *4.4.2 Impact of Image Processing Uncertainty on Pore Network Model* 210 *Output*

211 To establish a pore network modeling workflow that is as insulated from user sub-
 212 jectivity as possible, a robust image processing uncertainty analysis was performed on
 213 a subdomain ($333 \times 333 \times 333$ voxels = $2 \times 2 \times 2$ mm) of Core 1. The main sources of
 214 uncertainty can be categorized as image acquisition, image processing, pore network ex-
 215 traction, and pore network simulation parameterization. The output function used to
 216 evaluate uncertainty was the pore network model drainage capillary pressure curve. Ini-
 217 tial screening sensitivity of various segmentation methods, network extraction input, pore
 218 network simulation variables found that image processing had by far the greatest impact
 219 on this characteristic curve output relative to the other categories tested, and therefore
 220 was the focus of the uncertainty analysis. Different acquisition settings were not tested
 221 as these will be highly dependent on different micro-CT scanner hardware. While con-
 222 tact angle and interfacial tension are very important parameters in the network model
 223 simulation, these properties were well constrained from previous experimental studies
 224 with similar rock-fluid pairs (Lin et al., 2018; S. J. Jackson et al., 2019). For other rock-
 225 fluid pairs, there are extensive contact angle and interfacial tension datasets available
 226 in literature (e.g. Kazakov et al. (2012); Ethington (1990); Espinoza and Santamarina
 227 (2010)).

228 The three main steps in a typical image processing workflow are filtering/denoising,
 229 edge sharpening, and segmentation (i.e. the conversion of a grayscale image into a im-
 230 age with voxels categorized as air-rock in the dry scan, or water-decane-rock in the mul-
 231 tiphase flow scans). The filter methods tested were the Median 3D filter, the Non-local
 232 Means Denoising (Buades et al., 2005), and the Gaussian Blur 3D. Realizations either
 233 had no edge sharpening or used the Unsharpen Mask ImageJ plugin. The image segmen-
 234 tation algorithms tested included the Robust Automatic Threshold (RATS), the Otsu
 235 method, Statistical Region Merging, and a global threshold. The massive size of the ex-
 236 perimental datasets that needed to be efficiently processed prevented the use of more com-
 237 putationally expensive and sophisticated segmentation tools such as Weka or other machine-

238 learning based methods. All image processing was completed in the open-source image
 239 analysis/processing software FIJI/ImageJ.

240 To provide a robust analysis and extensive survey of the image processing param-
 241 eter space (i.e. the range of reasonable values for each image processing method), an au-
 242 tomated routine was written in Matlab to interface with FIJI via MIJ (Daniel Sage, Dimiter
 243 Prodanov & Schindelin, 2012). A nested sampling routine was used for mapping the im-
 244 age processing input of 1000 processed image realizations. An Excel sheet with specific
 245 parameter input ranges of each method is included in the Supporting Information (SI).

246 Following the segmentation of each realization, an automated post-processing ex-
 247 amination was performed to reject unphysical realizations. This examination was per-
 248 formed by sampling a small subregion of the image confidently known to be solid grain.
 249 If the segmented image contained any pore space in this subregion then the realization
 250 was rejected. The remaining 557 realizations were run through PNextract and PNflow
 251 by calling the executables from Matlab. All realizations were run with identical extrac-
 252 tion and flow settings. Of the resulting models, 373 remained after a final screening that
 253 rejected models with a porosity outside of the range of 0.17-0.221. This range was cho-
 254 sen based on an independent core-average clinical CT porosity (Akin & Kovscek, 2003)
 255 measurement for Core 1. A schematic overview of the analysis performed is provided in
 256 Figure S1 in the SI. The first slice of seven example segmented realizations are shown
 257 in Figure S2 in the SI. The first ten realizations, pore network input and output files,
 258 and Matlab scripts for method automation and pore network model interfacing are in-
 259 cluded in the data repository referenced in the Acknowledgements.

260 *4.4.3 Image Processing Workflow*

261 Based on the sensitivity analysis results (provided in Figure S3 in the SI), the im-
 262 age processing and pore network modeling workflows written in Matlab were adapted
 263 to process the entire datasets for each Bentheimer core. The workflow for the dry micro-
 264 CT data was as follows:

- 265 1. Raw normalized, merged, micro-CT images were filtered with the ImageJ Non-
 266 local Means Denoising.
- 267 2. Filtered images were segmented into air/rock binary images (e.g. top zoomed im-
 268 age in Figure 1). Segmentation was performed with a global threshold in ImageJ

269 chosen such that the porosity at the inlet of the core was equal to the indepen-
 270 dent porosity measurement. In this study we used a single measurement of poros-
 271 ity at the inlet of the cores taken from clinical CT porosity measurements. Anal-
 272 ogous independent porosity measurements could utilize Helium pycnometry or
 273 other measurement techniques on adjacent samples to the core.

- 274 3. Segmented images were discretized into separate smaller REV-scale 3D subdomains.
 275 The subdomains were $316 \times 316 \times 300$ and $316 \times 316 \times 318$ voxels in Core 1 and
 276 2, respectively. This corresponded to an approximately cubic pore network model
 277 and Darcy-model grid cell size with a side length equal to 1.896mm ($6\mu\text{m} \times 316$ vox-
 278 els). The REV side-length dimensions were determined from detailed REV anal-
 279 ysis performed by S. J. Jackson et al. (2019) and are in agreement with previous
 280 Bentheimer REV analysis (Halisch, 2013).
- 281 4. The porosity of the discretized subdomains was calculated by $\phi_i = \varphi_{air,i} / \varphi_{rock,i}$.
 282 Here $\varphi_{air,i}$ is the volume fraction segmented as air, and $\varphi_{rock,i}$ is the volume frac-
 283 tion segmented as rock.
- 284 5. Pore networks were extracted with PNextract from each subdomain segmented
 285 image.
- 286 6. Flow simulations were run on the extracted subdomains with PNflow.

287 Using a similar workflow, it was possible to measure local water saturation in the
 288 discretized subdomains for comparison with Darcy-scale model simulation output. The
 289 image processing workflow for the multiphase flow experiments was as follows:

- 290 1. Raw normalized, merged, micro-CT images were filtered with the ImageJ non-local
 291 means filter.
- 292 2. Filtered images were segmented into nonwetting phase/brine+rock binary images
 293 with a global threshold. The segmentation threshold value was determined from
 294 the minimum histogram value between the nonwetting phase (decane) and brine
 295 histogram peaks.
- 296 3. Segmented images were discretized into smaller subdomains identical in size to the
 297 dry scan discretization.
- 298 4. The water saturation of each subdomain i was calculated by $S_{w,i} = (1 - (\varphi_{nw,i} / \phi_i))$.
 299 Here $\varphi_{nw,i}$ is the volume fraction of nonwetting phase in the subdomain.

300 Water saturation measurement uncertainty was estimated by calculating subdo-
301 main water saturation on images segmented at thresholds plus and minus 5% of the grayscale
302 range relative to the histogram minimum established in step 2 (see histogram illustra-
303 tion in Figure S3 of the SI). Porosity, raw PNM output, and characteristic curve fits for
304 every subdomain of both rocks are provided in the data repository referenced in the Ac-
305 knowledgements.

306 4.5 Darcy-Scale Modeling

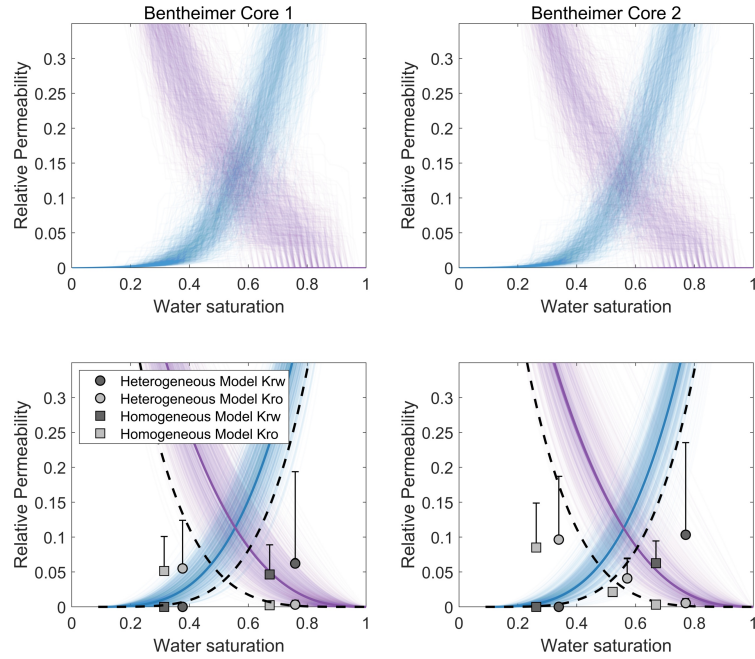
307 Darcy-scale multiphase simulation was performed with the Computer Modeling Group
308 (CMG) IMEX commercial reservoir simulator (Computer Modelling Group LTD, 2017).
309 The grid cell discretization was set to exactly match the processed image and pore-network
310 model dimensions (e.g. see saturation maps in Figure 1).

311 Four sets of simulations were run on each core. These were designed to test the rel-
312 ative importance of including heterogeneity in capillary pressure and relative permeabil-
313 ity characteristics, as derived from the pore network models. The first set of simulations
314 utilized a constant set of capillary pressure and relative permeability curves in every grid
315 cell—excluding the end slices, as described below. These models show the fluid satura-
316 tion distribution assuming the cores behave as homogeneous porous mediums. The sec-
317 ond set of simulations used PNM-derived capillary pressure and relative permeability curves
318 to parameterize the characteristic heterogeneity throughout the cores. These models high-
319 light the improved match between modeled saturation distribution and the experimen-
320 tal data when heterogeneity is characterized. The third set of simulations used PNM-
321 derived capillary pressure and a single relative permeability curve determined from the
322 mean of the PNM output to parameterize the characteristic heterogeneity throughout
323 the cores. These models demonstrate the limited influence of relative permeability char-
324 acterization on fluid saturation distribution. The final set of simulations used the same
325 heterogeneous characteristic curves but had a constant permeability value of 1000 mD
326 in both cores, rather than using the experimentally measured permeability of 1635 mD
327 and 763 mD in Core 1 and 2, respectively. These models emphasize that exact exper-
328 imental permeability measurements are not necessary to implement the workflow described
329 here.

330 In the homogeneous simulation models, the relative permeability curves were taken
 331 from previous experimental measurements on large core samples by S. J. Jackson et al.
 332 (2019) and C. Reynolds and Krevor (2015) (dashed black lines in Figure 2). These wet-
 333 ting and nonwetting phase relative permeability functions from previous work are de-
 334 fined by the modified Brooks-Corey functions $k_{rw} = ((S_w - S_{wir})/(1 - S_{wir}))^{4.4}$ and
 335 $k_{rnw} = k_{rnw,ir}(1 - (S_w - S_{w,ir})/(1 - S_{w,ir}))^{4.6}$, respectively. Here the nonwetting phase
 336 relative permeability at the irreducible water saturation is $k_{rnw,ir} = 0.8$. The irreducible
 337 water saturation is $S_{w,ir} = 0.08$. The homogeneous model capillary pressure curve was
 338 derived from the fluid-scaled MICP curve, represented by the yellow line shown in Fig-
 339 ure 3.

340 In the heterogeneous models of Core 1 and Core 2 pore network model output is
 341 used to define the capillary pressure and relative permeability of each grid cell. Based
 342 on the uncertainty analysis—and as observed by previous studies—the capillary pres-
 343 sure in the smallest pores at low wetting phase saturation has the highest uncertainty
 344 (Silin & Patzek, 2006; Berg et al., 2016). The most accurate portion of the pore network
 345 model capillary pressure prediction is at high water saturations (i.e. largest features in
 346 the micro-CT images). Therefore, the raw pore network model capillary pressure val-
 347 ues from $S_w = 0.8$ to $S_w = 0.9$ were used to scale the MICP curve via a linear least
 348 squares fitting method implemented in Matlab. The portion of the capillary pressure curve
 349 from $S_w = 0.9$ to $S_w = 1$ was not used for fitting because this portion of the curve is
 350 dependent on boundary conditions and pore network extraction definition. These bound-
 351 ary effects were found to decrease with increasing model/subdomain size, in agreement
 352 with previous modeling (Papafotiou et al., 2008; Raeini et al., 2019) and experimental
 353 studies (Norton & Knapp, 1977; Zahasky et al., 2018). This approach of scaling the MICP
 354 capillary pressure is similar to other approaches that use porosity/permeability/saturation
 355 relationships to scale local capillary entry pressure to define capillary heterogeneity (Krevor
 356 et al., 2011; Krause, 2012; B. Li & Benson, 2015). The raw and scaled capillary pres-
 357 sure curve for every grid cell in Core 2 are shown in Figure 3. The heterogeneous rel-
 358 ative permeability curves were defined by modified Brooks-Corey relative permeability
 359 curves fit to PNM output. A plot of the raw and fitted PNM relative permeability out-
 360 put for every subdomain in both cores is shown in Figure 2.

376 In all models the grid cell porosity was heterogeneous and determined directly from
 377 the segmented micro-CT image of the corresponding subdomain (i.e. step 4 of the dry



361 **Figure 2.** Raw pore network model relative permeability curves (top plots) and modified
 362 Brooks-Corey relative permeability functions fit to the raw output (bottom plots). The plots on
 363 the left illustrate the relative permeability in every subdomain in Core 1, while the plots on the
 364 right are for every subdomain in Core 2. The bold lines in the bottom plots illustrate the average
 365 of all of the PNM output. The dashed black lines were used to define the homogeneous simula-
 366 tion models and are based on experimental measurements in a number of Bentheimer samples
 367 from previous studies (S. J. Jackson et al., 2019; C. Reynolds & Krevor, 2015). The square points
 368 in the bottom plots indicate core-average relative permeability calculated in the fully homoge-
 369 nous CMG simulation model. The circular points in the bottom plots show the core-average
 370 relative permeability calculated from the fully heterogeneous CMG simulation model results.
 371 The vertical error bars on the simulation points illustrates the dominant impact of the boundary
 372 conditions on uncertainty in the estimate of pressure differential. The variation is a function of
 373 outlet slice capillary pressure at 0 kPa, 0.2 kPa (plotted points), and 3.7 kPa. The outlet slice
 374 capillary pressure has less influence on the core-average saturation measurements; the saturation
 375 variation is smaller than the size of the data markers.

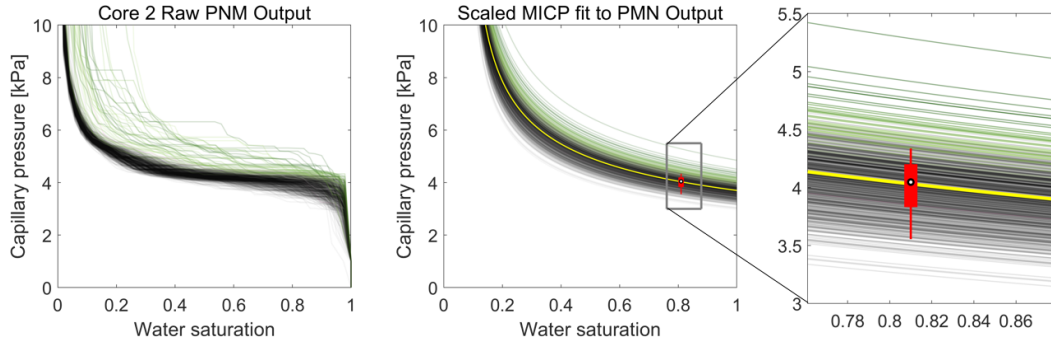
378 image workflow described above). To parameterize the model inlet and outlet face con-
 379 ditions, three inlet slices and three outlet slices were added to the portion of the mod-
 380 els defined by the scanned section of the cores. In all models, the first and last slices were
 381 set to replicate the experimental coreholder inlet and outlet caps. These had linear rel-
 382 ative permeability curves, permeability set an order of magnitude higher than the respec-
 383 tive core matrix permeability, and a constant capillary pressure of 0.2 kPa. Results of
 384 0 kPa and 3.7 kPa capillary pressure were also tested to illustrate the impact of the cap-
 385 illary end effect on the relative permeability uncertainty as shown in Figure 2. A cap-
 386 illary pressure of 0.2 kPa was used because this is the theoretical capillary pressure of
 387 the tubing entering and exiting the coreholder in the experiments (1.5875 mm OD, 0.7938
 388 mm ID). A capillary pressure of 3.7 kPa was chosen as an upper bounds because this
 389 is the average capillary entry pressure based on MICP analysis. Two additional slices
 390 were added to each end of the model to represent the unscanned portion of the core in
 391 the experiments. The relative permeability and capillary pressure curves in the unscanned
 392 slices were set to the average of the first and last model slices in the respective models.
 393 The full CMG model input and output files for both of the cores are available in the data
 394 repository referenced in the Acknowledgements.

395 5 Results

396 5.1 Pore Network Model Prediction of Capillary Heterogeneity

397 Core 2 was used for capillary heterogeneity analysis because dry image character-
 398 ization indicated the presence of a low porosity zone crosscutting the sample near the
 399 outlet end of the core. This feature is illustrated in Figure 1 as the low porosity zone in
 400 the porosity map plot. The raw and scaled pore network model capillary pressure curves
 401 of every subdomain in Core 2 are shown in Figure 3. The capillary pressure curves cor-
 402 responding to the low porosity capillary barrier are highlighted in green. The elevated
 403 capillary entry pressure predicted in this zone by the PNM is qualitatively confirmed by
 404 the experimental saturation measurements (Figure 1 *Experimental S_w* plot). The mea-
 405 sured saturation values indicate that this low porosity zone produced a capillary bar-
 406 rier that limited the invasion of nonwetting phase relative to the inlet of the core.

407 To confidently predict the capillary heterogeneity in porous media, the heterogene-
 408 ity must be greater than the uncertainty in image processing and fluid saturation mea-



416 **Figure 3.** (left) Example raw capillary pressure curve output (both green and black lines)
 417 from every subdomain of Core 2. (middle) Corresponding capillary pressure curves used for every
 418 grid cell in the CMG model based on scaling the MICP curve (yellow line) based on curve fitting
 419 described in Section 4.5. (right) A zoomed-in plot of the scaled MICP curves. The green lines
 420 highlight the capillary pressure curves corresponding to the low porosity/high entry pressure
 421 zone visible in Figure 1. Specifically, the subdomains with a porosity less than 20% are colored
 422 in green. For reference, the shade of green corresponds to the entry pressure colorbar in Figure
 423 1. The red box plot marks the range of uncertainty arising from the image processing workflow.
 424 The top and bottom of the thin red line indicate the 90th and 10th percentile results, found to
 425 be 3.56 kPa and 4.34 kPa, respectively. The top and bottom of the thick red line indicate the
 426 75th and 25th percentile results, found to be 3.83 kPa and 4.20 kPa, respectively. The dot in the
 427 middle is the median capillary pressure (4.05 kPa) determined from the uncertainty analysis. A
 428 plot showing all of the raw capillary pressure curves used to calculate these statistics is shown in
 429 Figure S3 in the SI.

409 measurements. A comparison between the uncertainty analysis results and the PNM cap-
 410 illary heterogeneity is indicated by the red boxplot on the center plot, and zoomed in-
 411 set to the right, in Figure 3. This comparison illustrates that the capillary pressure in
 412 nearly all the subdomains of the low porosity/capillary barrier zone in Core 2 (green lines)
 413 fall well above the bounds of uncertainty. This highlights that one of the key features
 414 necessary to predict and accurately simulate multiphase flow—capillary heterogeneity—
 415 can be determined with this pore network modeling workflow.

430 **5.2 Improvement in Darcy-Scale Model When Accounting for Capillary**
 431 **Heterogeneity**

432 A comparison between the experimentally measured water saturation and the wa-
 433 ter saturation from the CMG models is given for both cores in the right plots in Figure
 434 4. The slice average comparisons include both the results of the CMG simulation with
 435 heterogeneous grid cell capillary pressure and relative permeability (bold solid lines), and
 436 homogeneous characteristic curves (thin solid lines). The local saturation variation in
 437 the experimental data decrease at lower water fractional flow as the impact of subtle dif-
 438 ferences in capillary forces are suppressed. However, the experimental saturation mea-
 439 surement uncertainty (shaded grey region around dashed lines) increases with decreas-
 440 ing water saturation. This happens because the nonwetting phase interfaces are the main
 441 source of segmentation uncertainty. Therefore, the saturation measurement uncertainty
 442 increases as the nonwetting phase interfacial area and nonwetting phase saturation in-
 443 crease.

The left plots in Figure 4 provide a direct comparison between micro-CT subdo-
 main saturation and simulated saturations in every grid cell in the heterogeneous mod-
 els. To more quantitatively compare the results of the CMG model saturation in every
 grid cell ($S_{w,n}^{sim}$) to the experimental water saturation in the corresponding subdomain
 ($S_{w,n}^{exp}$), the mean relative saturation error ($\bar{\delta}_{Sw}$) in every subdomain/grid cell (n) and
 at all fractional flows was calculated with Equation 1.

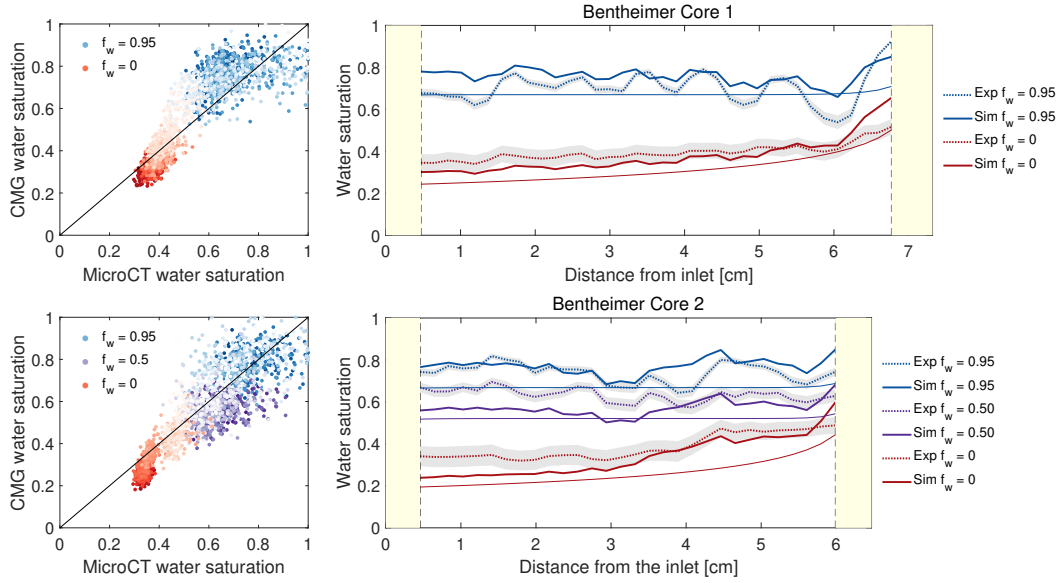
$$\bar{\delta}_{Sw} = \frac{1}{n} \sum_n \frac{|S_{w,n}^{exp} - S_{w,n}^{sim}|}{S_{w,n}^{exp}} \quad (1)$$

444 The mean grid cell relative saturation error for the homogeneous Core 1 CMG model at
 445 all fractional flows was 0.173 while the heterogeneous model using PNM input was 0.138.
 446 In the more heterogeneous Core 2, the homogeneous simulation model relative satura-
 447 tion error was 0.203 while the heterogeneous model was only 0.139. The improved sat-
 448 uration prediction in the heterogeneous models is due to a combination of more accu-
 449 rate local saturation prediction (e.g. the elevated water saturation behind the capillary
 450 barrier in Core 2) and the overestimation of nonwetting phase saturation in the homo-
 451 geneous models in both cores.

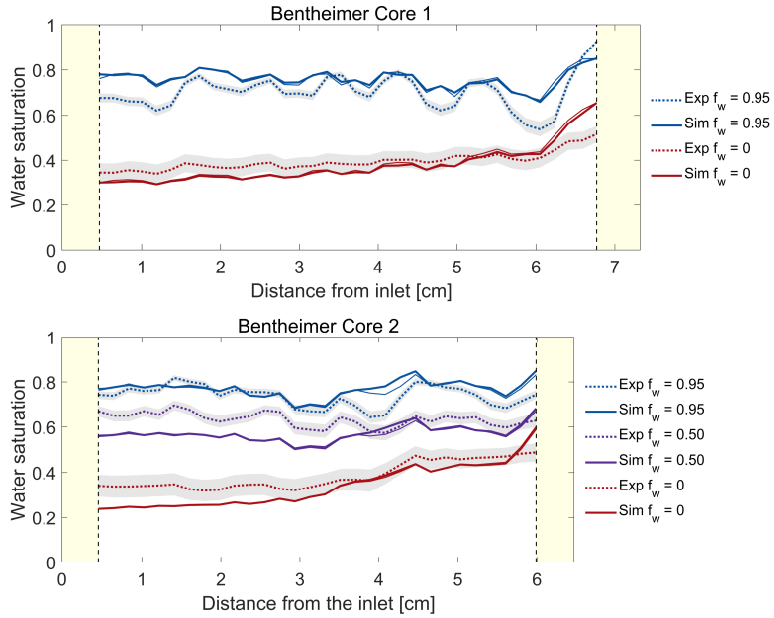
452 To further highlight the importance of capillary heterogeneity, Figure 5 compares
 453 the results of the fully heterogeneous model shown in Figure 4 with the simulation model
 454 that uses the same heterogeneous PNM capillary pressure curves but only a single rel-

455 active permeability curve. The single relative permeability curve is determined by tak-
 456 ing the average of the PNM relative permeability curves in the respective cores (bold col-
 457 ored lines in lower plots in Figure 2). The slice-average saturation profiles from the mod-
 458 els with homogeneous and heterogeneous relative permeability are nearly indistinguish-
 459 able in Figure 5. This highlights that the capillary pressure heterogeneity characteriza-
 460 tion is essential in systems where capillary forces dominate over viscous forces. In con-
 461 trast, heterogeneity in relative permeability characteristics contribute relatively little.
 462 This is likely due to the spatial character of the heterogeneity - where the heterogene-
 463 ity in capillary pressure characteristics is structured in layers, the heterogeneity in rel-
 464 ative permeability is distributed randomly. Thus a single, upscaled or average, relative
 465 permeability is sufficient in this case.

466 Both cores show a capillary end effect, particularly at low fractional flows of wa-
 467 ter. The capillary end effect describes the elevated water saturation near the outlet of
 468 the cores driven by a capillary pressure discontinuity at outlet face. The end effect is slightly
 469 stronger in Core 2 due to the capillary barrier described above. The simulated core-average
 470 relative permeability values are shown in Figure 2. As illustrated by the vertical error
 471 bars, the core-average relative permeability in the models is strongly influenced by the
 472 simulation parameterization approach to account for the capillary end effect. The ver-
 473 tical bars in Figure 2 show the change in core-average relative permeability when the in-
 474 let and outlet slice capillary pressure is set to 3.7 kPa rather than 0.2 kPa. The core-
 475 average relative permeability in the homogeneous model (square points in Figure 2) are
 476 lower than the local grid cell input (dashed black lines) at all fractional flow rates be-
 477 cause of the capillary end effect reduces the fluid mobility near the outlet of the core,
 478 particularly in the unscanned region. Despite the uncertainty in the core-average rela-
 479 tive permeability, the PNM subdomain relative permeability predictions are systemat-
 480 ically higher than the bulk experimental measurements. The implementation of these
 481 subdomain measurements in the heterogeneous models leads to core-average simulation
 482 relative permeability values (circular points in Figure 2) that agree better with the pre-
 483 vious experimental measurements than the homogeneous model relative permeability val-
 484 ues. This is because the aggregate effect of the multiphase heterogeneities is to lower the
 485 core-average relative permeability of the fluid phases below that of relative permeabil-
 486 ity of any of the individual subdomains.



487 **Figure 4.** Water saturation comparison between multiscale simulation predictions and exper-
 488 imental measurements for Core 1 (top plots), and Core 2 (bottom plots). The figures on the left
 489 illustrate direct micro-CT subdomain to simulation grid cell comparison. The color darkness cor-
 490 responds to the length along the core (e.g. dark red is near inlet and faint red is near the outlet).
 491 The figures on the right indicate the slice average saturations measured experimentally (dashed
 492 lines) and in the simulations (solid lines). The shaded grey region around the dashed lines in-
 493 dicates the saturation measurement uncertainty as described in the image processing workflow
 494 and shown in Figure S1 of the SI. The thick solid lines illustrate heterogeneous simulation re-
 495 sults using pore network model input. The thin solid lines illustrate the homogeneous simulation
 496 model results. The experimental saturation profile in Core 2 indicates how the capillary barrier
 497 limits drainage on the downstream side of the barrier, leading to an increase in water saturation
 498 approximately 4 cm from the inlet of the core. Note the ability of the heterogeneous simulation
 499 model to capture this feature, particularly at a water fractional flow of zero (see Figure 1 for
 500 center-slice saturation comparison). Water fractional flows (f_w) of 0.95, 0.5, and 0 are respec-
 501 tively represented by blue, purple, and red in all plots. The vertical dashed lines and the shaded
 502 yellow regions in the plots on the right indicate the unscanned portion of the cores.



503 **Figure 5.** Water saturation slice-average profile comparison between simulation models and
 504 experimental measurements for Core 1 and Core 2. The dashed lines are the slice-average satu-
 505 rations measured experimentally and the thick solid lines are the simulations with heterogeneous
 506 PNM-derived relative permeability and capillary pressure curves assigned to each grid cell. These
 507 are identical to the lines shown in Figure 4. The thin solid lines are simulations in each core
 508 using the mean PNM relative permeability (bold colored lines in lower plot in Figure 2) but the
 509 same heterogeneous capillary pressure curves as the model indicated by the bold solid lines. Note
 510 that the solid lines are nearly indistinguishable at every fractional flow. The vertical dashed lines
 511 and the shaded yellow regions in the plots on the right indicate the unscanned portion of the
 512 cores.

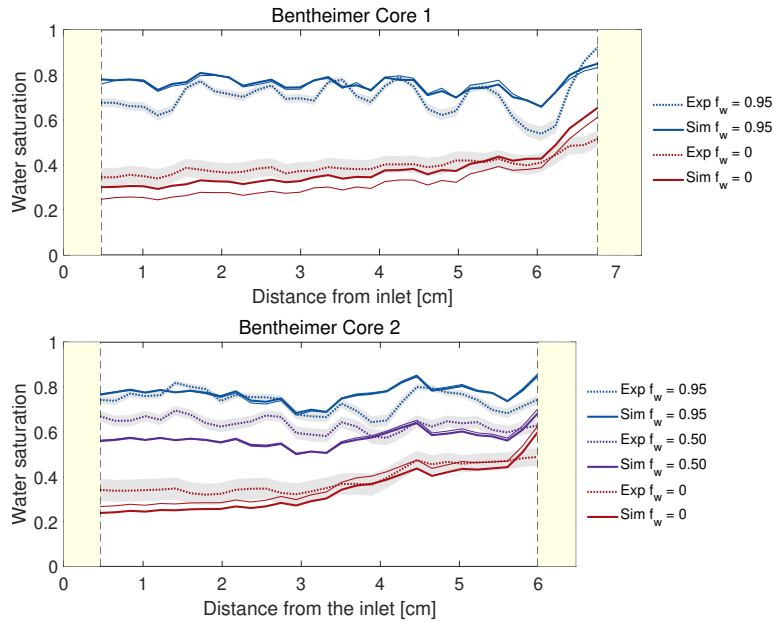
513 **5.3 Darcy-Scale Models With Limited Permeability Information**

514 To emphasize that exact experimental permeability measurements are not neces-
 515 sary to accurately reproduce experimental saturation measurements, two heterogeneous
 516 simulation models of each core are shown in Figure 6. The bold lines illustrate the CMG
 517 models that utilized single-phase flow-through permeability measurements of 1635 mD
 518 and 763 mD permeability in Core 1 and Core 2, respectively. The thin lines illustrate
 519 CMG simulations with the same heterogeneous relative permeability and capillary pres-
 520 sure derived from the pore network models, but with homogeneous permeability values
 521 of 1000 mD in both core samples. The slice-average saturation profiles in the models with
 522 different permeability only become distinguishable from each at very low water fractional
 523 flow. These results highlight that under the experimental conditions of this study, the
 524 saturation distributions are more sensitive to accurate capillary pressure characteriza-
 525 tion than to permeability parameterization.

536 **6 Discussion and Implications**

537 The characterization workflow proposed in this study opens the possibility for a
 538 digital workflow for estimating multiphase flow properties. In this workflow the most la-
 539 borious components of a core analysis work program—such as core flooding relative per-
 540 meability measurements—are no longer required. This is because the workflow utilizes
 541 only micro-CT images of dry cores, an independent measurement of porosity near the
 542 sample inlet (clinical CT), a MICP curve, and some knowledge—from literature or ex-
 543 perimental measurements—of the wettability and interfacial tension of the fluids in the
 544 system. The Darcy-scale model parameterized with heterogeneous PNM capillary pres-
 545 sure and relative permeability curves successfully captured subtle features of experimen-
 546 tal observations and provided a more accurate match to the experimental saturation data
 547 at every fractional flow than the homogeneous models neglecting capillary heterogene-
 548 ity.

549 The capillary pressure heterogeneity is the dominant mechanism controlling whole-
 550 core equivalent relative permeability and sub-core fluid saturation distribution at the cen-
 551 timeter length scale as shown in Figure 5. This may be in part because there is clear spa-
 552 tial structure to the heterogeneity in capillary pressure whereas heterogeneity in rela-



526 **Figure 6.** Water saturation slice-average profile comparison between simulation models and
 527 experimental measurements for Core 1 and Core 2. The dashed lines are the slice-average satu-
 528 rations measured experimentally and the thick solid lines are the simulations with 1635 mD and
 529 763 mD permeability in Core 1 and Core 2, respectively. These are identical to the lines shown
 530 in Figure 4. The thin solid lines are simulations in each core using 1000 mD homogeneous perme-
 531 ability but the same heterogenous characteristic curves as the model indicated by the bold solid
 532 lines. Note that at high water fractional flow the solid lines are nearly indistinguishable. The
 533 shaded grey region around the dashed lines indicates the saturation measurement uncertainty.
 534 The vertical dashed lines and the shaded yellow regions in the plots on the right indicate the
 535 unscanned portion of the cores.

553 tive permeability characteristics are randomly distributed. However, the exact relative
554 permeability structure cannot be conclusively determined without further investigation.

555 The importance of capillary heterogeneity is significant for a number of reasons.
556 As demonstrated by the sensitivity analysis (Figure S3 in the SI), pore network model
557 descriptions of capillary pressure are much less dependent on image processing uncer-
558 tainty than relative permeability. This is also significant because sub-core scale estimates
559 of capillary pressure characteristics can be validated by ganglia-curvature based mea-
560 surements (Herring et al., 2017; Garing et al., 2017; Lin et al., 2018, 2018; S. J. Jack-
561 son et al., 2019), whereas estimates of relative permeability across similar size domains
562 cannot.

563 The insensitivity of saturation distributions to absolute permeability demonstrated
564 in Figure 6 indicates that this workflow does not require exact permeability measure-
565 ments, but permeability could instead be approximated from literature values, relevant
566 porosity-permeability relationships (Tiab & Donaldson, 2016), or possibly pore network
567 modeling. While the pore network model output could be used to define the Darcy-scale
568 permeability, the uncertainty analysis performed here agrees with previous studies that
569 found permeability is highly sensitive to image processing (Beckingham et al., 2013; Guan
570 et al., 2018). Conceptually this is because permeability calculations in pore network mod-
571 els are dominated by the smallest features of the sample, and thus are very uncertain
572 without model calibration. These observations agree with other work demonstrating the
573 importance of capillary pressure characterization rather than permeability characteri-
574 zation for accurate multiphase flow modeling at low capillary numbers (Corbett et al.,
575 1992; Krause, 2012; B. Li & Benson, 2015; S. Jackson et al., 2018).

576 We highlight that the capillary pressure of sample subdomains can be determined
577 from image characterization of the capillary entry pressure. While the maximal ball method
578 implemented in the PNextract open-source network extraction algorithm was used in this
579 study, any number of open-source or commercial geometric or pore-scale modeling ap-
580 proaches could be used to estimate capillary entry pressure. The uncertainty analysis
581 and simulation results indicate that pore network model capillary entry pressure esti-
582 mates are accurate and relatively insulated from the image processing decisions because
583 these measurements are based on the largest pore features in the images. When com-
584 pared with the magnitude of a relatively subtle capillary barrier in the Bentheimer sand-

585 stone Core 2, the increase in capillary entry pressure in this feature was clearly differ-
586 entiable from the bounds of image processing uncertainty.

587 Pore network modeling has several technical and practical advantageous over tra-
588 ditional multiphase flow characterization approaches. First, traditional approaches are
589 impacted by experimental artifacts, such as the capillary end effects, as described in de-
590 tail in Figure 2. Another advantage of using PNM to characterize capillary heterogene-
591 ity is that measurements are not influenced by viscous forces that are typically ignored
592 with assumptions of capillary equilibrium across the system (Krause et al., 2013; Pini
593 & Benson, 2013, 2017; S. J. Jackson et al., 2018; Hosseinzadeh Hejazi et al., 2019). In
594 circumventing the need for expensive and time-consuming experimental characterization,
595 this digital approach mitigates key practical barriers to incorporating small-scale cap-
596 illary heterogeneity into reservoir simulation upscaling workflows.

597 It is important to reemphasize that the multiphase simulation model input presented
598 and compared with the experimental data was sourced from an uncalibrated pore net-
599 work model, assuming some knowledge of fluid contact angle and interfacial tension. As
600 a result of this calibration-free approach, we have illustrated a predictive multiscale char-
601 acterization workflow. This work provides a new way to rapidly estimate characteristic
602 relative permeability and capillary pressure data without the need for flow-through ex-
603 periments. More rapid and economical characterization will significantly improve numer-
604 ical models of complex fluid flow processes in the subsurface. Improved multiphase mod-
605 els are essential for better predictions of complex multiphase flow problems such as global-
606 scale carbon mitigation with geologic carbon sequestration, contaminate migration and
607 remediation, and invasion of pollutants into the vadose zone.

608 **Acknowledgments**

609 Supplemental data is available on the British Geological Survey National Geoscience Data
610 Centre at doi.org/10.5285/4483646c-6e21-4927-a2bf-60f9648e6dec.

611 Funding for this work was provided by ACT ELEGANCY, Project No 271498, has
612 received funding from DETEC (CH), BMWi (DE), RVO (NL), Gassnova (NO), BEIS
613 (UK), Gassco, Equinor and Total, and is cofunded by the European Commission under
614 the Horizon 2020 programme, ACT Grant Agreement No 691712. Samuel Jackson re-
615 ceived funding from the Natural Environment Research Council, Grant number: NE/N016173/1.

616 **References**

- 617 Akin, S., & Kovscek, A. (2003). Computed Tomography in Petroleum Engineer-
 618 ing Research. *Applications of X-ray Computed Tomography in the Geosciences*,
 619 *215*, 23–38.
- 620 Al-Khulaifi, Y., Lin, Q., Blunt, M. J., & Bijeljic, B. (2019). Pore-Scale Dissolution
 621 by CO₂ Saturated Brine in a Multimineral Carbonate at Reservoir Conditions:
 622 Impact of Physical and Chemical Heterogeneity. *Water Resources Research*,
 623 *55*(4), 3171–3193. doi: 10.1029/2018WR024137
- 624 Al-Menhali, A. S., & Krevor, S. (2016). Capillary Trapping of CO₂ in Oil Reser-
 625 voirs: Observations in a Mixed-Wet Carbonate Rock. *Environmental Science*
 626 *and Technology*, *50*(5), 2727–2734. doi: 10.1021/acs.est.5b05925
- 627 Armstrong, R. T., Porter, M. L., & Wildenschild, D. (2012). Linking pore-scale
 628 interfacial curvature to column-scale capillary pressure. *Advances in Wa-*
 629 *ter Resources*, *46*, 55–62. Retrieved from [http://dx.doi.org/10.1016/](http://dx.doi.org/10.1016/j.advwatres.2012.05.009)
 630 [j.advwatres.2012.05.009](http://dx.doi.org/10.1016/j.advwatres.2012.05.009) doi: 10.1016/j.advwatres.2012.05.009
- 631 Arns, C. H., Knackstedt, M. A., Pinczewski, W. V., & Lindquist, W. B. (2001). Ac-
 632 curate estimation of transport properties from microtomographic images. *Geo-*
 633 *physics Research Letters*, *28*(17), 3361–3364.
- 634 Bakke, S., & Øren, P.-E. (1997). 3-D Pore-Scale Modelling of Sandstones and Flow
 635 Simulations in the Pore Networks. *SPE Journal*, *2*(02), 136–149. doi: 10.2118/
 636 35479-pa
- 637 Bartels, W., Rücker, M., Boone, M., Bultreys, T., Mahani, H., Berg, S., ... Cnudde,
 638 V. (2019). Imaging spontaneous imbibition in full Darcyscale samples at
 639 porescale resolution by fast Xray tomography. *Water Resources Research*, *Ac-*
 640 *cepted*, 1–29. Retrieved from [https://onlinelibrary.wiley.com/doi/abs/](https://onlinelibrary.wiley.com/doi/abs/10.1029/2018WR024541)
 641 [10.1029/2018WR024541](https://onlinelibrary.wiley.com/doi/abs/10.1029/2018WR024541) doi: 10.1029/2018WR024541
- 642 Beekingham, L. E., Peters, C. A., Um, W., Jones, K. W., & Lindquist, W. B.
 643 (2013). 2D and 3D imaging resolution trade-offs in quantifying pore throats
 644 for prediction of permeability. *Advances in Water Resources*, *62*, 1–12. doi:
 645 10.1016/j.advwatres.2013.08.010
- 646 Beekingham, L. E., Steefel, C. I., Swift, A. M., Voltolini, M., Yang, L., Anovitz,
 647 L. M., ... Xue, Z. (2017). Evaluation of accessible mineral surface areas for
 648 improved prediction of mineral reaction rates in porous media. *Geochimica et*

- 649 *Cosmochimica Acta*, 205, 31–49. doi: 10.1016/j.gca.2017.02.006
- 650 Berg, S., Rücker, M., Ott, H., Georgiadis, A., van der Linde, H., Enzmann, F., ...
 651 Wiegmann, A. (2016). Connected pathway relative permeability from pore-
 652 scale imaging of imbibition. *Advances in Water Resources*, 90, 24–35. doi:
 653 10.1016/j.advwatres.2016.01.010
- 654 Berg, S., Saxena, N., Shaik, M., & Pradhan, C. (2018). Generation of ground truth
 655 images to validate micro-CT image-processing pipelines. *The Leading Edge*,
 656 37(6), 412–420. doi: 10.1190/tle37060412.1
- 657 Bijeljic, B., Muggeridge, A. H., & Blunt, M. J. (2004). Pore-scale modeling of lon-
 658 gitudinal dispersion. *Water Resources Research*, 40(11), 1–9. doi: 10.1029/
 659 2004WR003567
- 660 Blunt, M., & King, P. (1991). Relative Permeabilities from Two-and Three-
 661 Dimensional Pore-Scale Network Modelling. *Transport in Porous Media*,
 662 6, 407–433. Retrieved from [https://link.springer.com/content/pdf/](https://link.springer.com/content/pdf/10.1007/BF00136349.pdf)
 663 [10.1007/BF00136349.pdf](https://link.springer.com/content/pdf/10.1007/BF00136349.pdf)
- 664 Blunt, M. J. (1997). *Effects of Heterogeneity and Wetting on Relative Permeability*
 665 *Using Pore Level Modeling* (Vol. 2). doi: SPE36762
- 666 Buades, A., Coll, B., & Morel, J. M. (2005). A non-local algorithm for image denois-
 667 ing. *Proceedings - 2005 IEEE Computer Society Conference on Computer Vi-*
 668 *sion and Pattern Recognition, CVPR 2005, II(0)*, 60–65. doi: 10.1109/CVPR
 669 .2005.38
- 670 Bultreys, T., De Boever, W., & Cnudde, V. (2016). Imaging and image-based fluid
 671 transport modeling at the pore scale in geological materials: A practical intro-
 672 duction to the current state-of-the-art. *Earth-Science Reviews*, 155, 93–128.
 673 Retrieved from <http://dx.doi.org/10.1016/j.earscirev.2016.02.001>
 674 doi: 10.1016/j.earscirev.2016.02.001
- 675 Bultreys, T., Lin, Q., Gao, Y., Raeini, A. Q., Alratrout, A., Bijeljic, B., & Blunt,
 676 M. J. (2018). Validation of model predictions of pore-scale fluid distri-
 677 butions during two-phase flow. *Physical Review E*, 97(5). doi: 10.1103/
 678 PhysRevE.97.053104
- 679 Chaudhary, K., Bayani Cardenas, M., Wolfe, W. W., Maisano, J. A., Ketcham,
 680 R. A., & Bennett, P. C. (2013). Pore-scale trapping of supercritical CO₂ and
 681 the role of grain wettability and shape. *Geophysical Research Letters*, 40(15),

- 682 3878–3882. doi: 10.1002/grl.50658
- 683 Chen, J. D., & Wilkinson, D. (1985). Pore-scale viscous fingering in porous me-
684 dia. *Physical Review Letters*, *55*(18), 1892–1895. doi: 10.1103/PhysRevLett.55
685 .1892
- 686 Computer Modelling Group LTD. (2017). *IMEX Three-phase, Black-oil Reservoir*
687 *Simulator*. Calgary, Alberta Canada: Computer Modelling Group LTD.
- 688 Corbett, P. W. M., Ringrose, P. S., Jensen, J. L., & Sorbie, K. S. (1992). Lami-
689 nated clastic reservoirs: The interplay of capillary pressure and sedimentary
690 architecture. *Proceedings - SPE Annual Technical Conference and Exhibition*,
691 365–376.
- 692 Cowton, L. R., Neufeld, J. A., White, N. J., Bickle, M. J., Williams, G. A., White,
693 J. C., & Chadwick, R. A. (2018). Benchmarking of vertically-integrated
694 CO₂ flow simulations at the Sleipner Field, North Sea. *Earth and Planetary*
695 *Science Letters*, *491*, 121–133. Retrieved from [https://doi.org/10.1016/](https://doi.org/10.1016/j.epsl.2018.03.038)
696 [j.epsl.2018.03.038](https://doi.org/10.1016/j.epsl.2018.03.038) doi: 10.1016/j.epsl.2018.03.038
- 697 Daniel Sage, Dimiter Prodanov, J.-Y. T., & Schindelin, J. (2012). MIJ: Making In-
698 teroperability Between ImageJ and Matlab Possible. In *Imagej user & devel-*
699 *oper conference*. Luxembourg.
- 700 De Chalendar, J. A., Garing, C., & Benson, S. M. (2018). Pore-scale modelling of
701 Ostwald ripening. *Journal of Fluid Mechanics*, *835*, 363–392. doi: 10.1017/jfm
702 .2017.720
- 703 Dong, H., & Blunt, M. J. (2009). Pore-network extraction from micro-computerized-
704 tomography images. *Physical Review E*, *80*(3), 036307. Retrieved
705 from <https://link.aps.org/doi/10.1103/PhysRevE.80.036307> doi:
706 10.1103/PhysRevE.80.036307
- 707 Eiken, O., Ringrose, P., Hermanrud, C., Nazarian, B., Torp, T. A., & Høier,
708 L. (2011). Lessons Learned from 14 years of CCS Operations: Sleip-
709 ner, In Salah and Snøhvit. *Energy Procedia*, *4*, 5541–5548. doi: 10.1016/
710 j.egypro.2011.02.541
- 711 Espinoza, D. N., & Santamarina, J. C. (2010). Water-CO₂-mineral systems: Interfa-
712 cial tension, contact angle, and diffusion Implications to CO₂ geological storage.
713 *Water Resources Research*, *46*(7), 1–10. doi: 10.1029/2009WR008634
- 714 Ethington, E. F. (1990). *Interfacial contact angle measurements of water, mer-*

- 715 *cury, and 20 organic liquids on quartz, calcite, biotite, and Ca-montmorillonite*
 716 *substrates* (Tech. Rep. No. July). doi: 10.1016/j.conbuildmat.2005.09.001
- 717 Feehley, C. E., Zheng, C., & Molz, F. J. (2000). A dual-domain mass transfer ap-
 718 proach for modeling solute transport in heterogeneous aquifers: Application
 719 to the macrodispersion experiment (MADE) site. *Water Resources Research*,
 720 *36*(9), 2501–2515. doi: 10.1029/2000WR900148
- 721 Garing, C., de Chalendar, J. A., Voltolini, M., Ajo-Franklin, J. B., & Benson,
 722 S. M. (2017). Pore-scale capillary pressure analysis using multi-scale X-
 723 ray micromotography. *Advances in Water Resources*, *104*, 223–241. Re-
 724 trieved from <http://dx.doi.org/10.1016/j.advwatres.2017.04.006> doi:
 725 10.1016/j.advwatres.2017.04.006
- 726 Guan, K. M., Guo, B., Creux, P., Kovscek, A. R., Tchelepi, H., & Nazarova, M.
 727 (2018). Effects of Image Resolution on Sandstone Porosity and Permeability as
 728 Obtained from X-Ray Microscopy. *Transport in Porous Media*, *127*(1), 233–
 729 245. Retrieved from <https://doi.org/10.1007/s11242-018-1189-9> doi:
 730 10.1007/s11242-018-1189-9
- 731 Guice, K., Lun, L., Gao, B., Gupta, R., Gupta, G., Kralik, J. G., . . . Jawhari, A.
 732 (2014). An Evaluation of Digital Rock Physics Technology for the Prediction
 733 of Relative Permeability and Capillary Pressure for a Middle Eastern Carbon-
 734 ate Reservoir. *International Petroleum Technology Conference, IPTC 17288*,
 735 1–11.
- 736 Halisch, M. (2013). The Rev Challenge Estimating Representative Elementary Vol-
 737 umes and Porous Rock Inhomogeneity From High Resolution Micro-Ct Data
 738 Sets. *Society of Core Analysts*(069), 1–7.
- 739 Herring, A. L., Harper, E. J., Andersson, L., Sheppard, A., Bay, B. K., & Wilden-
 740 schild, D. (2013). Effect of fluid topology on residual nonwetting phase
 741 trapping: Implications for geologic CO₂ sequestration. *Advances in Wa-*
 742 *ter Resources*, *62*, 47–58. Retrieved from <http://dx.doi.org/10.1016/j.advwatres.2013.09.015> doi: 10.1016/j.advwatres.2013.09.015
- 744 Herring, A. L., Middleton, J., Walsh, R., Kingston, A., & Sheppard, A. (2017).
 745 Flow rate impacts on capillary pressure and interface curvature of connected
 746 and disconnected fluid phases during multiphase flow in sandstone. *Advances*
 747 *in Water Resources*, *107*, 460–469. Retrieved from <http://dx.doi.org/>

- 748 10.1016/j.advwatres.2017.05.011 doi: 10.1016/j.advwatres.2017.05.011
- 749 Hilpert, M., & Miller, C. T. (2001). Pore-morphology-based simulation of drainage
750 in totally wetting porous media. *Advances in Water Resources*, 24(3-4), 243–
751 255. doi: 10.1016/S0309-1708(00)00056-7
- 752 Hosseinzadeh Hejazi, S. A., Shah, S., & Pini, R. (2019). Dynamic measurements
753 of drainage capillary pressure curves in carbonate rocks. *Chemical Engineer-
754 ing Science*, 200, 268–284. Retrieved from [https://www.sciencedirect.com/
755 science/article/pii/S0009250919301356?via=ihub](https://www.sciencedirect.com/science/article/pii/S0009250919301356?via=ihub) doi: 10.1016/J
756 .CES.2019.02.002
- 757 Hussain, F., Pinczewski, W. V., Cinar, Y., Arns, J. Y., Arns, C. H., & Turner, M. L.
758 (2014). Computation of Relative Permeability from Imaged Fluid Distribu-
759 tions at the Pore Scale. *Transport in Porous Media*, 104(1), 91–107. doi:
760 10.1007/s11242-014-0322-7
- 761 Idowu, N. A., & Blunt, M. J. (2010). Pore-scale modelling of rate effects in water-
762 flooding. *Transport in Porous Media*, 83(1), 151–169. doi: 10.1007/s11242-009
763 -9468-0
- 764 Iglauer, S., Fernø, M. A., Shearing, P., & Blunt, M. J. (2012). Comparison of
765 residual oil cluster size distribution, morphology and saturation in oil-wet and
766 water-wet sandstone. *Journal of Colloid and Interface Science*, 375(1), 187–
767 192. Retrieved from <http://dx.doi.org/10.1016/j.jcis.2012.02.025> doi:
768 10.1016/j.jcis.2012.02.025
- 769 Jackson, S., Mayachita, I., & Krevor, S. (2018). High resolution modelling
770 and steady-state upscaling of large scale gravity currents in heteroge-
771 neous sandstone reservoirs. *5th CO2 Geological Storage Workshop, 2018-
772 Novem*(November 2018).
- 773 Jackson, S. J., Agada, S., Reynolds, C. A., & Krevor, S. (2018). Characterizing
774 Drainage Multiphase Flow in Heterogeneous Sandstones. *Water Resources Re-
775 search*, 54(4), 3139–3161. doi: 10.1029/2017WR022282
- 776 Jackson, S. J., Lin, Q., & Krevor, S. (2019). Representative elementary volumes,
777 hysteresis and heterogeneity in multiphase flow from the pore to continuum
778 scale. *Submitted and available on EarthArXiv*(22 September), 1–33. Retrieved
779 from <https://eartharxiv.org/2aejr/>
- 780 Jerauld, G. R., & Salter, S. J. (1990). The Effect of Pore Structure on Hysteresis in

- 781 Relative Permeability and Capillary Pressure: Pore Level Modeling. *Transport*
782 *in Porous Media*, 5, 103.
- 783 Jiang, Z., Wu, K., Couples, G., Van Dijke, M. I., Sorbie, K. S., & Ma, J. (2007). Ef-
784 ficient extraction of networks from three-dimensional porous media. *Water Re-*
785 *sources Research*, 43(12), 1–17. doi: 10.1029/2006WR005780
- 786 Joekar-Niasar, V., Prodanović, M., Wildenschild, D., & Hassanizadeh, S. M. (2010).
787 Network model investigation of interfacial area, capillary pressure and satura-
788 tion relationships in granular porous media. *Water Resources Research*, 46(6),
789 1–18. doi: 10.1029/2009WR008585
- 790 Kang, P. K., Lee, J., Fu, X., Lee, S., Peter K. Kitanidis, & Juanes, R. (2017). Im-
791 proved characterization of heterogeneous permeability in saline aquifers from
792 transient pressure data during freshwater injection. *Water Resources Research*,
793 53, 4444–4458. doi: 10.1002/2016WR020089. Received
- 794 Kazakov, A., Muzny, C. D., Kroenlein, K., Diky, V., Chirico, R. D., Magee, J. W.,
795 ... Frenkel, M. (2012). NIST/TRC source data archival system: The next-
796 generation data model for storage of thermophysical properties. *International*
797 *Journal of Thermophysics*, 33(1), 22–33. doi: 10.1007/s10765-011-1107-7
- 798 Krause, M. (2012). Modeling and investigation of the influence of capillary hetero-
799 geneity on relative permeability. *SPE Annual Technical Conference and Exhibi-*
800 *tion*(October), 8–10. Retrieved from [https://www.onepetro.org/conference](https://www.onepetro.org/conference-paper/SPE-160909-STU)
801 [-paper/SPE-160909-STU](https://www.onepetro.org/conference-paper/SPE-160909-STU)
- 802 Krause, M., Krevor, S., & Benson, S. M. (2013). A Procedure for the Accurate
803 Determination of Sub-Core Scale Permeability Distributions with Error Quan-
804 tification. *Transport in Porous Media*, 98(3), 565–588.
- 805 Krevor, S. C. M., Pini, R., Li, B., & Benson, S. M. (2011, aug). Capillary het-
806 erogeneity trapping of CO₂ in a sandstone rock at reservoir conditions. *Geo-*
807 *physical Research Letters*, 38(15), n/a–n/a. Retrieved from [http://doi.wiley](http://doi.wiley.com/10.1029/2011GL048239)
808 [.com/10.1029/2011GL048239](http://doi.wiley.com/10.1029/2011GL048239) doi: 10.1029/2011GL048239
- 809 Lai, P., Moulton, K., & Krevor, S. (2015). Pore-scale heterogeneity in the mineral
810 distribution and reactive surface area of porous rocks. *Chemical Geology*, 411,
811 260–273. Retrieved from [http://dx.doi.org/10.1016/j.chemgeo.2015.07](http://dx.doi.org/10.1016/j.chemgeo.2015.07.010)
812 [.010](http://dx.doi.org/10.1016/j.chemgeo.2015.07.010) doi: 10.1016/j.chemgeo.2015.07.010
- 813 Lenormand, R., Touboul, E., & Zarcone, C. (1988). NUmberical models and ex-

- 814 periments on immiscible displacements in porous media. *Journal of Fluid*
815 *Mechanics*, 189(C), 165–187. Retrieved from [papers3://publication/uuid/](https://doi.org/10.1007/s11242-014-0378-4)
816 [500C8DAA-9E14-45CC-A2EF-5CCBEA82D161](https://doi.org/10.1007/s11242-014-0378-4)
- 817 Leu, L., Berg, S., Enzmann, F., Armstrong, R. T., & Kersten, M. (2014). Fast X-
818 ray Micro-Tomography of Multiphase Flow in Berea Sandstone: A Sensitivity
819 Study on Image Processing. *Transport in Porous Media*, 105(2), 451–469. doi:
820 [10.1007/s11242-014-0378-4](https://doi.org/10.1007/s11242-014-0378-4)
- 821 Li, B., & Benson, S. M. (2015). Influence of small-scale heterogeneity on upward
822 CO₂ plume migration in storage aquifers. *Advances in Water Resources*, 83,
823 389–404. doi: [10.1016/j.advwatres.2015.07.010](https://doi.org/10.1016/j.advwatres.2015.07.010)
- 824 Li, J., McDougall, S. R., & Sorbie, K. S. (2017). Dynamic pore-scale network model
825 (PNM) of water imbibition in porous media. *Advances in Water Resources*,
826 107, 191–211. doi: [10.1016/j.advwatres.2017.06.017](https://doi.org/10.1016/j.advwatres.2017.06.017)
- 827 Li, T., Schlüter, S., Dragila, M. I., & Wildenschild, D. (2018). An improved method
828 for estimating capillary pressure from 3D microtomography images and its
829 application to the study of disconnected nonwetting phase. *Advances in Wa-*
830 *ter Resources*, 114, 249–260. Retrieved from [https://doi.org/10.1016/](https://doi.org/10.1016/j.advwatres.2018.02.012)
831 [j.advwatres.2018.02.012](https://doi.org/10.1016/j.advwatres.2018.02.012) doi: [10.1016/j.advwatres.2018.02.012](https://doi.org/10.1016/j.advwatres.2018.02.012)
- 832 Lin, Q., Al-Khulaifi, Y., Blunt, M. J., & Bijeljic, B. (2016). Quantification of
833 sub-resolution porosity in carbonate rocks by applying high-salinity contrast
834 brine using X-ray microtomography differential imaging. *Advances in Water*
835 *Resources*, 96, 306–322. doi: [10.1016/j.advwatres.2016.08.002](https://doi.org/10.1016/j.advwatres.2016.08.002)
- 836 Lin, Q., Bijeljic, B., Berg, S., Pini, R., Blunt, M. J., & Krevor, S. (2019). Min-
837 imal surfaces in porous media: Pore-scale imaging of multiphase flow in an
838 altered-wettability Bentheimer sandstone. *Physical Review E*, 99(6), 1–13. doi:
839 [10.1103/PhysRevE.99.063105](https://doi.org/10.1103/PhysRevE.99.063105)
- 840 Lin, Q., Bijeljic, B., Pini, R., Blunt, M. J., & Krevor, S. (2018). Imaging and mea-
841 surement of pore-scale interfacial curvature to determine capillary pressure
842 simultaneously with relative permeability. *Water Resources Research*, 7046–
843 7060. Retrieved from <http://doi.wiley.com/10.1029/2018WR023214> doi:
844 [10.1029/2018WR023214](https://doi.org/10.1029/2018WR023214)
- 845 Lindquist, W. B., Coker, D. A., Spanne, P., Lee, S.-M., & Jones, K. W. (2004).
846 Medial axis analysis of void structure in three-dimensional tomographic im-

- 847 ages of porous media. *Journal of Geophysical Research: Solid Earth*, 101(B4),
848 8297–8310. doi: 10.1029/95jb03039
- 849 Mason, G., & Morrow, N. R. (1991). Capillary behavior of a perfectly wetting liquid
850 in irregular triangular tubes. *Journal of Colloid And Interface Science*, 141(1),
851 262–274. doi: 10.1016/0021-9797(91)90321-X
- 852 Mehmani, Y., & Tchelepi, H. A. (2017). Minimum requirements for predictive pore-
853 network modeling of solute transport in micromodels. *Advances in Water Re-*
854 *sources*, 108, 83–98. Retrieved from [https://doi.org/10.1016/j.advwatres](https://doi.org/10.1016/j.advwatres.2017.07.014)
855 .2017.07.014 doi: 10.1016/j.advwatres.2017.07.014
- 856 Menke, H. P., Bijeljic, B., Andrew, M. G., & Blunt, M. J. (2015). Dynamic three-
857 dimensional pore-scale imaging of reaction in a carbonate at reservoir con-
858 ditions. *Environmental Science and Technology*, 49(7), 4407–4414. doi:
859 10.1021/es505789f
- 860 Nguyen, V. H., Sheppard, A. P., Knackstedt, M. A., & Val Pinczewski, W. (2006).
861 The effect of displacement rate on imbibition relative permeability and residual
862 saturation. *Journal of Petroleum Science and Engineering*, 52(1-4), 54–70. doi:
863 10.1016/j.petrol.2006.03.020
- 864 Norton, D., & Knapp, R. (1977). Transport phenomena in hydrothermal sys-
865 tems: The nature of porosity. *American Journal of Science*, 277, 913–936.
866 Retrieved from [papers2://publication/uuid/F03A8A4C-B5FD-4004-8493](https://publication/uuid/F03A8A4C-B5FD-4004-8493-CBFA884B7133)
867 -CBFA884B7133
- 868 Øren, P. E., Ruspini, L. C., Saadatfar, M., Sok, R. M., Knackstedt, M., & Herring,
869 A. (2019). In-situ pore-scale imaging and image-based modelling of capillary
870 trapping for geological storage of CO₂ International Journal of Greenhouse
871 Gas Control In-situ pore-scale imaging and image-based modelling of capil-
872 lary trapping for geological storage of . *International Journal of Greenhouse*
873 *Gas Control*, 87(May), 34–43. Retrieved from [https://doi.org/10.1016/](https://doi.org/10.1016/j.ijggc.2019.04.017)
874 [j.ijggc.2019.04.017](https://doi.org/10.1016/j.ijggc.2019.04.017) doi: 10.1016/j.ijggc.2019.04.017
- 875 Papafotiou, A., Helmig, R., Schaap, J., Lehmann, P., Kaestner, A., Fluhler, H., . . .
876 Durner, W. (2008). From the pore scale to the lab scale: 3-D lab experiment
877 and numerical simulation of drainage in heterogeneous porous media. *Advances*
878 *in Water Resources*, 31(9), 1253–1268. doi: 10.1016/j.advwatres.2007.09.006
- 879 Pianosi, F., Beven, K., Freer, J., Hall, J. W., Rougier, J., Stephenson, D. B., &

- 880 Wagener, T. (2016). Sensitivity analysis of environmental models: A sys-
 881 tematic review with practical workflow. *Environmental Modelling and*
 882 *Software*, 79, 214–232. Retrieved from [http://dx.doi.org/10.1016/](http://dx.doi.org/10.1016/j.envsoft.2016.02.008)
 883 [j.envsoft.2016.02.008](http://dx.doi.org/10.1016/j.envsoft.2016.02.008) doi: 10.1016/j.envsoft.2016.02.008
- 884 Pini, R., & Benson, S. M. (2013). Characterization and scaling of mesoscale hetero-
 885 geneities in sandstones. *Geophysical Research Letters*, 40(15), 3903–3908. doi:
 886 10.1002/grl.50756
- 887 Pini, R., & Benson, S. M. (2017). Capillary pressure heterogeneity and hysteresis
 888 for the supercritical CO₂/water system in a sandstone. *Advances in Water*
 889 *Resources*, 108, 277–292. Retrieved from [http://linkinghub.elsevier.com/](http://linkinghub.elsevier.com/retrieve/pii/S0309170817304189)
 890 [retrieve/pii/S0309170817304189](http://linkinghub.elsevier.com/retrieve/pii/S0309170817304189) doi: 10.1016/j.advwatres.2017.08.011
- 891 Raeini, A. Q., Bijeljic, B., & Blunt, M. J. (2015). Modelling capillary trapping using
 892 finite-volume simulation of two-phase flow directly on micro-CT images. *Ad-*
 893 *vances in Water Resources*, 83, 102–110. Retrieved from [http://dx.doi.org/](http://dx.doi.org/10.1016/j.advwatres.2015.05.008)
 894 [10.1016/j.advwatres.2015.05.008](http://dx.doi.org/10.1016/j.advwatres.2015.05.008) doi: 10.1016/j.advwatres.2015.05.008
- 895 Raeini, A. Q., Bijeljic, B., & Blunt, M. J. (2017). Generalized network modeling:
 896 Network extraction as a coarse-scale discretization of the void space of porous
 897 media. *Physical Review E*, 96(1), 1–17. doi: 10.1103/PhysRevE.96.013312
- 898 Raeini, A. Q., Bijeljic, B., & Blunt, M. J. (2018). Generalized network modeling of
 899 capillary-dominated two-phase flow. *Physical Review E*, 97(2). doi: 10.1103/
 900 PhysRevE.97.023308
- 901 Raeini, A. Q., Yang, J., Bondino, I., Bultreys, T., Blunt, M. J., & Bijeljic, B.
 902 (2019). Validating the Generalized Pore Network Model Using Micro-
 903 CT Images of Two-Phase Flow. *Transport in Porous Media*. Retrieved
 904 from <http://link.springer.com/10.1007/s11242-019-01317-8> doi:
 905 10.1007/s11242-019-01317-8
- 906 Rajaram, H., Ferrand, L. A., & Celia, M. A. (1997). Prediction of relative perme-
 907 abilities for unconsolidated soils using pore-scale network models. *Water Re-*
 908 *sources Research*, 33(1), 43–52. doi: 10.1029/96WR02841
- 909 Reynolds, C., & Krevor, S. (2015). Characterizing flow behavior for gas in-
 910 jection: Relative permeability of CO₂-brine and N₂-water in heteroge-
 911 neous rocks. *Water Resources Research*, 50, 9464–9489. doi: 10.1002/
 912 2015WR017273.Received

- 913 Reynolds, C. A., Blunt, M. J., & Krevor, S. (2018). Multiphase Flow Character-
 914 istics of Heterogeneous Rocks From CO₂ Storage Reservoirs in the United
 915 Kingdom. *Water Resources Research*, *54*, 729–745. Retrieved from [http://](http://doi.wiley.com/10.1002/2017WR021651)
 916 doi.wiley.com/10.1002/2017WR021651 doi: 10.1002/2017WR021651
- 917 Reynolds, C. A., Menke, H., Andrew, M., Blunt, M. J., & Krevor, S. (2017). Dy-
 918 namic fluid connectivity during steady-state multiphase flow in a sandstone.
 919 *Proceedings of the National Academy of Sciences*, *114*(31), 8187–8192. Re-
 920 trieved from <http://www.pnas.org/lookup/doi/10.1073/pnas.1702834114>
 921 doi: 10.1073/pnas.1702834114
- 922 Ringrose, P., Atbi, M., Mason, D., Espinassous, M., Myhrer, b., Myhrer, Ø., ...
 923 Wright, I. (2009). Plume development around well KB-502 at the In
 924 Salah CO₂ storage site. *First Break*, *27*(7005), 85–89. Retrieved from
 925 [http://www.earth.uwaterloo.ca/graduate/courses/earth691-duss/](http://www.earth.uwaterloo.ca/graduate/courses/earth691-duss/C02{_}GeneralC02Sequestrationmaterilas/C02{_}FBJan09{_}spectop5-1.pdf)
 926 [C02{_}GeneralC02Sequestrationmaterilas/C02{_}FBJan09{_}spectop5](http://www.earth.uwaterloo.ca/graduate/courses/earth691-duss/C02{_}GeneralC02Sequestrationmaterilas/C02{_}FBJan09{_}spectop5-1.pdf)
 927 [-1.pdf](http://www.earth.uwaterloo.ca/graduate/courses/earth691-duss/C02{_}GeneralC02Sequestrationmaterilas/C02{_}FBJan09{_}spectop5-1.pdf)
- 928 Ringrose, P. S., Sorbie, K. S., Corbett, P. W., & Jensen, J. L. (1993). Immis-
 929 sible flow behaviour in laminated and cross-bedded sandstones. *Jour-*
 930 *nal of Petroleum Science and Engineering*, *9*(2), 103–124. doi: 10.1016/
 931 0920-4105(93)90071-L
- 932 Sheng, Q., & Thompson, K. (2016). A unified pore-network algorithm for dy-
 933 namic two-phase flow. *Advances in Water Resources*, *95*, 92–108. Re-
 934 trieved from <http://dx.doi.org/10.1016/j.advwatres.2015.12.010> doi:
 935 10.1016/j.advwatres.2015.12.010
- 936 Silin, D., & Patzek, T. (2006). Pore space morphology analysis using maximal in-
 937 scribed spheres. *Physica A: Statistical Mechanics and its Applications*, *371*(2),
 938 336–360. doi: 10.1016/j.physa.2006.04.048
- 939 Singh, A., Armstrong, R., Regenauer-Lieb, K., & Mostaghimi, P. (2018). Rock
 940 characterization using Gray-Level Co-occurrence Matrix: An objective per-
 941 spective of digital rock statistics. *Water Resources Research*(2009). doi:
 942 10.1029/2018wr023342
- 943 Singh, V., Cavanagh, A., Hansen, H., Nazarian, B., Iding, M., & Ringrose, P. (2010).
 944 Reservoir modeling of CO₂ plume behavior calibrated against monitoring data
 945 from sleipner, Norway. *Proceedings - SPE Annual Technical Conference and*

- 946 *Exhibition*, 5, 3461–3479.
- 947 Tiab, D., & Donaldson, E. C. (2016). Porosity and Permeability. In *Petro-*
 948 *physics -theory and practice of measuring reservoir rock and fluid transport*
 949 *properties* (4th ed., pp. 67–186). San Francisco: Elsevier. Retrieved from
 950 <http://linkinghub.elsevier.com/retrieve/pii/B978012397021300017X>
 951 doi: 10.1016/B978-0-12-397021-3.00017-X
- 952 Valvatne, P. H., & Blunt, M. J. (2004). Predictive pore-scale modeling of two-phase
 953 flow in mixed wet media. *Water Resources Research*, 40(7), 1–21. doi: 10
 954 .1029/2003WR002627
- 955 Vogel, H.-J., Tölke, J., Schulz, V. P., Krafczyk, M., & Roth, K. (2005). Comparison
 956 of a Lattice-Boltzmann Model, a Full-Morphology Model, and a Pore Network
 957 Model for Determining Capillary Pressure Saturation Relationships. *Vadose*
 958 *Zone Journal*, 4(2), 380. doi: 10.2136/vzj2004.0114
- 959 Wildenschild, D., & Sheppard, A. P. (2013). X-ray imaging and analysis tech-
 960 niques for quantifying pore-scale structure and processes in subsurface
 961 porous medium systems. *Advances in Water Resources*, 51, 217–246. Re-
 962 trieved from <http://dx.doi.org/10.1016/j.advwatres.2012.07.018> doi:
 963 10.1016/j.advwatres.2012.07.018
- 964 Zahasky, C., & Benson, S. M. (2018). Micro-Positron Emission Tomography for
 965 Measuring Sub-core Scale Single and Multiphase Transport Parameters in
 966 Porous Media. *Advances in Water Resources*, 115, 1–16. Retrieved from
 967 <http://linkinghub.elsevier.com/retrieve/pii/S030917081731182X> doi:
 968 10.1016/j.advwatres.2018.03.002
- 969 Zahasky, C., Thomas, D., Matter, J., Maher, K., & Benson, S. M. (2018). Multi-
 970 modal imaging and stochastic percolation simulation for improved quantifi-
 971 cation of effective porosity and surface area in vesicular basalt. *Advances in*
 972 *Water Resources*, 121(June), 235–244. Retrieved from [https://doi.org/](https://doi.org/10.1016/j.advwatres.2018.08.009)
 973 [10.1016/j.advwatres.2018.08.009](https://doi.org/10.1016/j.advwatres.2018.08.009) doi: 10.1016/j.advwatres.2018.08.009
- 974 Zhao, B., MacMinn, C. W., Primkulov, B. K., Chen, Y., Valocchi, A. J., Zhao,
 975 J., ... Juanes, R. (2019). Comprehensive comparison of pore-scale models
 976 for multiphase flow in porous media. *Proceedings of the National Academy*
 977 *of Sciences of the United States of America*, 116(28), 13799–13806. doi:
 978 10.1073/pnas.1901619116